Measurement of coherent J/ψ in ultraperipheral Pb+Pb collisions at $\sqrt{s_{\mathrm{NN}}} = 5.36$ TeV with the ATLAS detector

P. Rybczyński [a]
on behalf of the ATLAS Collaboration

AGH University of Krakow, al. Adama Mickiewicza 30, 30-059 Kraków, Poland

The fully stripped ions used in heavy-ion collisions at the LHC are an excellent source of high-energy quasi-real photons. These can interact with photons emitted by the oncoming nucleus, or with the nucleus itself, either directly in inelastic processes or diffractively via pomeron exchange. Diffractive photonuclear processes can produce exclusive vector mesons that are uniquely sensitive to the spatial and momentum structure of the nuclear parton distribution functions, as well as spatial fluctuations (hotspots). In Run 3, the ATLAS experiment utilized a low-multiplicity track trigger in heavy-ion collisions for the first time, allowing the collection of a large sample of events with a few tracks. A substantial fraction of these events are dilepton decays of vector mesons, including the J/ψ. This paper presents the first ATLAS results on J/ψ differential cross section measurement as a function of J/ψ rapidity.

DOI: https://doi.org/10.17161/zmz88s41
Keywords: J/psi, coherent, upc, photoproduction, heavy-ion, ATLAS

1 Introduction

The physics and phenomenology of ultra-peripheral collisions (UPC), in particular vector meson photoproduction, are reviewed in Refs. [1,2]. Exclusive vector meson photoproduction can proceed in two ways: coherent or incoherent. In coherent photoproduction, the color-neutral exchanged object, typically referred to as a "pomeron", is emitted coherently by all the nucleons in the nucleus. This process does not resolve the nuclear structure directly, however it is sensitive to the average nuclear parton distribution function (nPDF). In contrast, in incoherent photoproduction, the pomeron is emitted by an individual nucleon, which leads to the nuclear breakup. Also a dissociative production is possible, where the pomeron couples to nucleon's partonic constituents. This leads to the dissociation of the nucleus. Coherent and incoherent exclusive processes can be differentiated experimentally using the magnitude of the transverse momentum (p_{T}) of the produced vector meson. This quantity is inversely related to the transverse size of the "target", i.e. the object struck by the photon. Coherent photoproduction involves the entire nucleus, and typically results in vector mesons with low transverse momentum (of about 50 MeV). Incoherent processes yield mesons with higher transverse momenta, around 250 MeV for photoproduction off of nucleons and 600 MeV for dissociative production. In the case of coherent interactions, the nuclei generally remain intact, although the strong electromagnetic fields of ultrarelativistic heavy nuclei can induce additional breakup through Coulomb dissociation, causing one or both nuclei to become excited and emit forward-going nucleons. Conversely, incoherent photoproduction typically leads to nuclear breakup, sometimes with the emission of additional forward hadrons, which can be misidentified as an exclusive process due to limited detector acceptance.

Charmonium photoproduction in Pb+Pb UPC has been studied widely by experiments at RHIC [3] and the LHC. Both the ALICE [4,5,6] and CMS Collaborations [7] have performed measurements at a nucleon–nucleon (NN) center-of-mass energy of $\sqrt{s_{\mathrm{NN}}} = 2.76$ TeV, in complementary J/ψ rapidity regions. ALICE has performed measurements near midrapidity ($|y| < 0.8$) with both dimuon and dielectron final states, and at forward rapidities $2.5 < y < 4$ with dimuons. CMS has measured the dimuon final state with $1.6 < |y| < 2.4$. In LHC Run 2, with $\sqrt{s_{\mathrm{NN}}} = 5.02$ TeV, updated measurements were made by ALICE[8,9,10] CMS [11], and LHCb [12,13], the latter in the forward region $2 < y < 4.5$.

In this analysis [14], the exclusive $J/\psi \to \mu^+\mu^-$ photoproduction cross section in Pb+Pb UPC at $\sqrt{s_{\mathrm{NN}}} = 5.36$ TeV is measured using 78 $\mu\mathrm{b}^{-1}$ of Run 3 data recorded in 2023. This is the first J/ψ measurement performed with the ATLAS detector. The muons are expected to lose all of their energy in the ATLAS calorimeter material before reaching the muon detectors. Moreover, electrons from the $J/\psi \to e^+e^-$ process are not considered as signal due to the poor electron energy resolution and identification efficiency in the relevant kinematic range. As a result, no specific muon or electron identification criteria

[a]Speaker, email: pawel.rybczynski@cern.ch

©Copyright 2025 CERN for the benefit of the ATLAS Collaboration. Reproduction of this article or parts of it is allowed as specified in the CC-BY-4.0 license.

are applied. Instead, the analysis relies on the reconstruction of a dimuon invariant mass from a pair of opposite-sign charged particles that are assumed to be muons. After removal of all known backgrounds, the J/ψ cross sections are measured differentially as a function of rapidity within $|y| < 2.5$. This new measurement complements the previous Run 2 measurements performed by other experiments, covering a previously unmeasured region $0.8 < y < 1.6$. The measured cross sections are compared with theoretical predictions, particularly those that incorporate parton saturation at low Bjorken-x [15,16]. Comparison with the measurements performed at $\sqrt{s_{\mathrm{NN}}} = 5.02$ TeV by the other collaborations [10,11,13] is made after a model-dependent extrapolation to account for the beam energy difference.

2 Detector

The ATLAS experiment [17,18] at the LHC is a multipurpose particle detector with a forward–backward symmetric cylindrical geometry and nearly 4π coverage in solid angle. It consists of an inner tracking detector (ID), electromagnetic and hadronic calorimeters, and a muon spectrometer. The ID is also surrounded by a thin superconducting solenoid providing an axial magnetic field. The ID covers the $|\eta| < 2.5$ pseudorapidity range. It consists of silicon pixel, silicon microstrip, and transition radiation tracking (TRT) detectors and can be sensitive to particles with p_{T} as low as 0.1 GeV [17].

The TRT is the outermost part of the ID, and it measures charged particle trajectories before they enter the calorimeters. It is built up of barrel and endcap modules corresponding to four η regions: barrel A ($0 < \eta \lesssim 0.8$), barrel C ($-0.8 \lesssim \eta < 0$), endcap A ($0.8 \lesssim \eta \lesssim 2.0$) and endcap C ($-2.0 \lesssim \eta \lesssim 0.8$).

Lead/liquid-argon (LAr) sampling calorimeters provide EM energy measurements with high granularity within the $|\eta| < 3.2$ region. A steel/scintillator-tile hadronic calorimeter covers the central pseudorapidity range of $|\eta| < 1.7$.

The endcap and forward (FCal) regions are instrumented with LAr calorimeters for EM and hadronic energy measurements up to $|\eta| = 4.9$. Forward neutrons produced from the breakup of lead nuclei in both hadronic and electromagnetic interactions are measured by compact tungsten sampling Zero Degree Calorimeters (ZDCs) positioned at $z = \pm 140$ meters from the ATLAS interaction point.

As the final state of $J/\psi \to \mu^+\mu^-$ consists of two soft muons, each with a p_{T} of about 1.5 GeV, the analysis primarily makes use of the ID. In particular, to trigger on the desired final state with two low momentum tracks, the TRT "FastOR" trigger is used at level 1 (L1) [19]. Its logic is illustrated in Figure 1 for the TRT barrel A region. The trigger algorithm performs a logical "OR" of fast electronic signals that are generated if a particle passes through a TRT straw tube. The TRT straw tubes are connected to the readout electronics via front-end modules. Each TRT front-end module processes signals from 16 straws and can be configured to send a signal to the TRT trigger timing and control (TTC) board if a hit exceeding a high threshold (HT) is recorded in any of its associated straws. A logic circuit on the TTC board aggregates these signals from front-end chip groups, corresponding to contiguous azimuthal regions. If the number of received signals within a TTC board exceeds a configurable threshold, set to four in 2023 Pb+Pb collisions, a trigger signal is generated. All four TRT regions provide similar binary trigger signals, which are logically OR'ed to provide a fast binary trigger decision for each event.

Typically, the TRT HT level is calibrated to the transition radiation threshold and is used for electron identification [20]. However, for the 2023 heavy-ion run, it was lowered to about twice the low threshold used in the standard tracking algorithms [20], so that a typical charged particle reaching the TRT produces multiple HT hits. This modification allows the TRT to efficiently trigger on events with low-momentum tracks, at the cost of its electron identification capabilities.

3 Data and Monte Carlo simulation samples

This analysis uses data recorded by the ATLAS detector in 2023 during Pb+Pb heavy-ion collisions at $\sqrt{s_{\mathrm{NN}}} = 5.36$ TeV.

At L1, the trigger decision relied on a positive signal from the TRT FastOR trigger, together with a veto on total transverse energy in calorimeters above 20 GeV. This selection rejected events with large hadronic activity, while ensuring there is some activity in the ID. At HLT, a veto on transverse energy in FCal above 5 GeV was applied. Also at least one (and no more than five) track with $p_{\mathrm{T}} > 1$ GeV was required. Furthermore, events with more than 15 low-p_{T} tracks (with $p_{\mathrm{T}} > 0.1$ GeV) are rejected. The data set recorded with these requirements corresponds to an integrated luminosity of 78 μb^{-1}.

Simulated Monte Carlo (MC) events for the signal coherent $J/\psi \to \mu^+\mu^-$ and background processes: coherent $J/\psi \to e^+e^-$, incoherent $J/\psi \to \ell^+\ell^-$, $\gamma\gamma \to \ell^+\ell^-$ were all generated using STARlight [21] interfaced with Pythia 8 [22] for simulation of QED final state radiation (FSR) [23]. Feed-down background

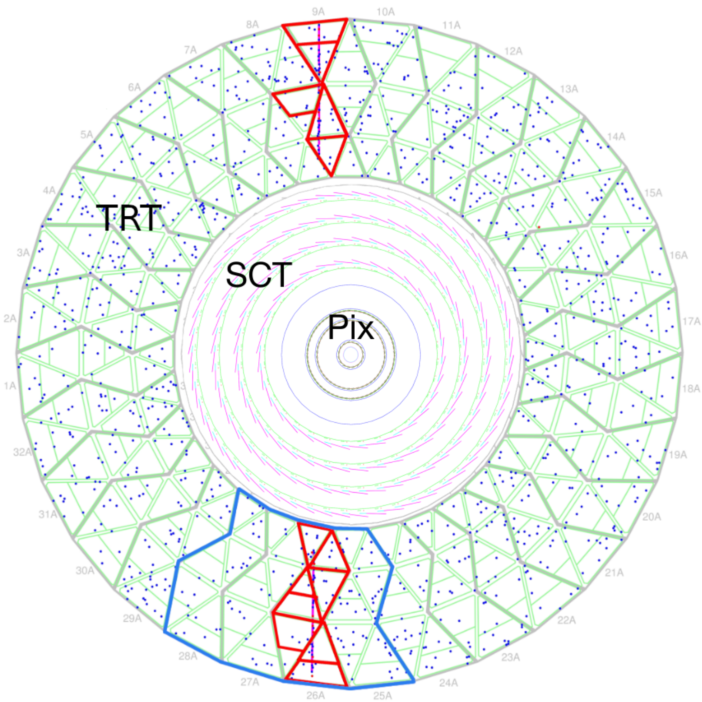

Figure 1 – The L1 TRT trigger logic in the TRT barrel A region ($0 < \eta \lesssim 0.8$) [19]. The region is divided into 32 ϕ sectors (bold gray), each consisting of 9 TRT trigger segments (shown as green triangles and trapezoids). A trigger signal within a segment is formed if the transition radiation threshold is exceeded in any of TRT straws from this segment (shown as red triangles and trapezoids, induced by a vertical cosmic track in this event). The trigger logic then aggregates signals from all segments in a region formed from four adjacent phi sectors (shown in blue), yielding an effective ϕ segmentation of $2\pi/8$. To form a trigger decision for this TRT section, the number of segments with a trigger signal has to exceed a fixed threshold multiplicity ($M = 4$) in at least one contiguous set of four sectors.

from coherent and incoherent $\psi(2S)$ were generated with STARlight, while EvtGen 2.2.1 [24] was used to provide $\psi(2S)$ decay channels. The FSR from the charged decay products of $\psi(2S)$ vector meson was simulated with Photos++ 3.61 [25].

4 Event selection

In the event selection exactly two tracks of opposite-charge are required. The event is rejected if there are more than two tracks with $p_{\mathrm{T}} > 0.1$ GeV and $|\eta| < 2.5$, that pass a loose track-quality selection. Both of the selected tracks are required to have $p_{\mathrm{T}} > 1$ GeV and a transverse impact parameter $|d_0| < 2$ mm. Muon mass hypothesis is used for the tracks. The signal region (SR) selection requires the dimuon system to have an invariant mass in the range $2.9 < m_{\mu^+\mu^-} < 3.2$ GeV, and pair transverse momentum $p_{\mathrm{T}}^{\mu^+\mu^-} < 0.2$ GeV.

5 Background estimation and signal yield extraction

The main background for the coherent $J/\psi \to \mu^+\mu^-$ are $J/\psi \to e^+e^-$ and $\gamma\gamma \to \ell^+\ell^-$, as well as incoherent $J/\psi \to \ell^+\ell^-$ processes, feed-down $\psi(2S)$ and inelastic photonuclear processes.

5.1 $\psi(2S)$ feed-down

The $\psi(2S)$ can decay into a J/ψ meson and other particles, which can remain undetected due to their low energy. This contribution is constrained through a normalization factor extracted from a 4-track control region, targeting the $\psi(2S) \to J/\psi(\to \ell^+\ell^-)\pi^+\pi^-$ process.

5.2 Inelastic hadronic processes

Due to the lack of muon identification, contamination from inelastic hadronic photonuclear processes is possible. In such events, some of the produced particles can be observed in the ID and mimic the signal. This background is modeled using a data-driven technique, where two tracks with same-sign charge are selected. A $p_{\mathrm{T}}^{\mu^+\mu^-}$ distribution template is created using a similar selection as for the signal, except that the opposite-sign requirement is replaced with a same-sign requirement These templates cover the range $p_{\mathrm{T}}^{\mu^+\mu^-} < 2$ GeV in the invariant mass region $2.9 < m_{\mu^+\mu^-} < 3.2$ GeV. Additionally the low-mass ($2.6 < m_{\mu^+\mu^-} < 2.75$ GeV) and high-mass ($3.25 < m_{\mu^+\mu^-} < 3.4$ GeV) sideband regions are used for normalization and as a cross-check. In these sidebands, the J/ψ contribution is suppressed, and the $\gamma\gamma \to \ell^+\ell^-$ background contributes only in the lower $p_{\mathrm{T}}^{\mu^+\mu^-}$ region. For this reason, the $p_{\mathrm{T}}^{\mu^+\mu^-} > 1$ GeV yield from the low-mass sideband can be used to normalize the same-sign $p_{\mathrm{T}}^{\mu^+\mu^-}$ template in the signal region, and in the high-mass sideband region for a cross-check. Figure 2 shows the low-mass and high-mass sidebands in the $0.5 < |y| < 1$ rapidity interval. An identical procedure is performed for each rapidity interval.

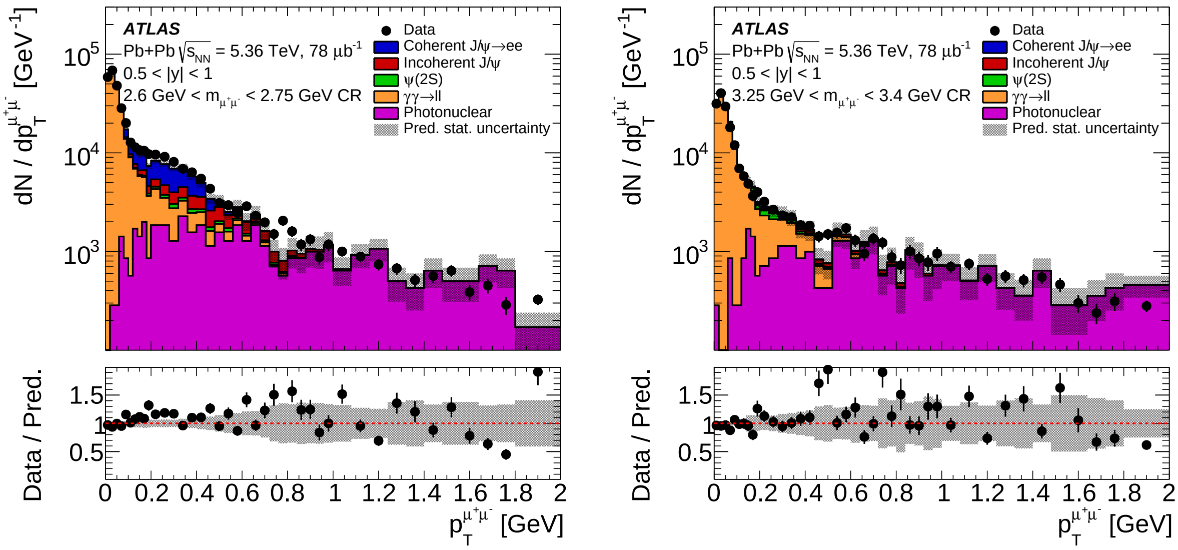

Figure 2 – Observed exclusive two-track system p_{T} distributions together with fitted signal and background contributions in the rapidity range $0.5 < |y| < 1$ for low-mass $2.6 < m_{\mu^+\mu^-} < 2.75$ GeV (left plot) and high-mass $3.25 < m_{\mu^+\mu^-} < 3.4$ GeV (right plot) sideband regions[14]. The photonuclear background templates are normalized in the low-mass sideband region in the $p_{\mathrm{T}}^{\mu^+\mu^-} > 1$ GeV range. The signal contribution (coherent $J/\psi \to \mu^+\mu^-$) is negligible in these two regions and hence it is not shown. For the calculation of $p_{\mathrm{T}}^{\mu^+\mu^-}$, the muon mass hypothesis is used for each track.

5.3 Fit to invariant mass

Due to low momenta of observed particles ($p_{\mathrm{T}} \sim 1.5$ GeV), they cannot reach the muon spectrometer, and no proper muon identification is possible. Thus, the $J/\psi \to \mu^+\mu^-$ and $J/\psi \to e^+e^-$ processes must be distinguished solely by differences in invariant mass shape distributions. Electrons experience significant distortions due to energy losses and radiative processes in the ID material. This results in an increased width of the $J/\psi \to e^+e^-$ peak and its shift towards lower invariant masses.

This discrimination is achieved with a fit to the two-track invariant mass spectrum in an extended mass range of $2.5 < m_{\mu^+\mu^-} < 3.5$ GeV. This fit also allows the estimation of $\gamma\gamma \to \ell^+\ell^-$ background contribution in the SR. In these fits, the $J/\psi \to e^+e^-$ and $J/\psi \to \mu^+\mu^-$ processes are modeled using double-sided Crystal Ball functions, whose parameters were fixed using fits to simulated events. The $\gamma\gamma \to \ell^+\ell^-$ background is modeled with an exponential function whose slope parameter is floating. A small contribution from inclusive photonuclear processes is also modeled with an exponential function fitted to a same-sign template from data. These fits are performed separately for each rapidity interval. Figure 3 presents the invariant mass distribution for the $|y| < 0.5$ rapidity interval and the fit results.

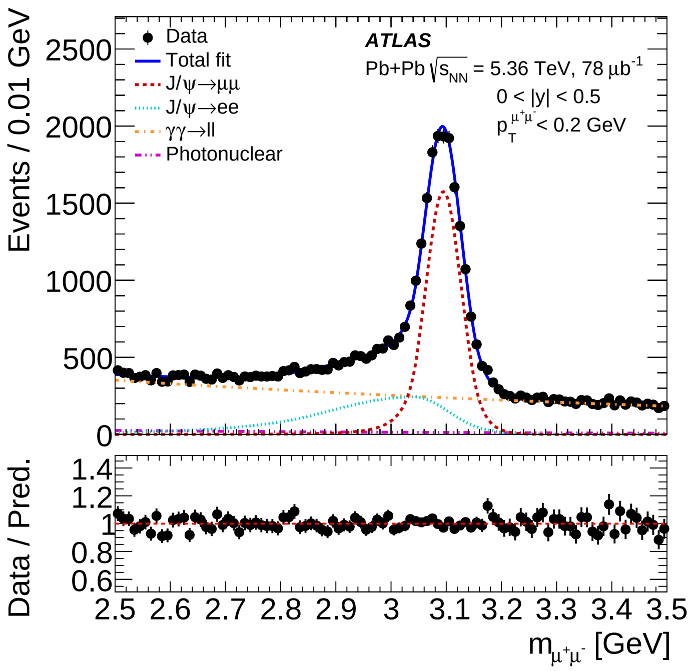

Figure 3 – Exclusive two-track invariant mass ($m_{\mu^+\mu^-}$) distribution for $|y| < 0.5$ interval [14]. Resonant contributions from $J/\psi \to \mu^+\mu^-$ and $J/\psi \to e^+e^-$ processes are shown as red and light-blue dashed lines, respectively. Non-resonant contributions from $\gamma\gamma \to \ell^+\ell^-$ and photonuclear backgrounds are shown as orange and magenta dashed lines respectively. The total fit result is shown as a solid blue line. For the calculation of $m_{\mu^+\mu^-}$, the muon mass hypothesis is used for each track. The signal region is defined as $2.9 < m_{\mu^+\mu^-} < 3.2$ GeV.

5.4 Fit to p_{T} spectrum

The coherent contribution to the J/ψ yield can be separated from the incoherent one using fits to the $p_{\mathrm{T}}^{\mu^+\mu^-}$ spectrum. For each rapidity interval, the $p_{\mathrm{T}}^{\mu^+\mu^-}$ distribution in the $2.9 < m_{\mu^+\mu^-} < 3.2$ GeV signal region is fitted with MC templates. Templates describing coherent and incoherent $J/\psi \to \ell^+\ell^-$, the dilepton continuum from the $\gamma\gamma \to \ell^+\ell^-$ process, and feed-down $J/\psi \to \ell^+\ell^-$ from decays of coherent and incoherent $\psi(2S)$ decays are created using the simulated STARlight events. Incoherent $J/\psi \to \ell^+\ell^-$ production with nucleon dissociation is described using the formula $d\sigma/dp_{\mathrm{T}} \approx p_{\mathrm{T}}(1 + (b_{pd}/n)p_{\mathrm{T}}^2)^{-n}$, where the parameters are set to $n = 3.58$ and $b_{pd} = 1.79$ GeV^{-2}, according to fits to $\gamma p \to J/\psi X$ data [26]. This functional form has been used in previous ALICE and CMS measurements [8,9,10,11].

In these fits, the contributions from $\psi(2S)$ and photonuclear processes are fixed according to the procedures explained in Section 5.1 and Section 5.2. The dilepton continuum $\gamma\gamma \to \ell^+\ell^-$ yield is fixed according to the results from fit to the invariant mass. The $e^+e^-/\mu^+\mu^-$ ratio is also fixed from the fit to the invariant mass. As a result, the only free parameters in the fit to the $p_{\mathrm{T}}^{\mu^+\mu^-}$ spectrum are the yields of coherent $J/\psi \to \ell^+\ell^-$, incoherent $J/\psi \to \ell^+\ell^-$, and dissociative $J/\psi \to \ell^+\ell^-$. For each rapidity interval, binned maximum-likelihood fits are performed for events in the $p_{\mathrm{T}}^{\mu^+\mu^-} < 2$ GeV range. Figure 4 shows the resulting $p_{\mathrm{T}}^{\mu^+\mu^-}$ distribution after the fit in the $|y| < 0.5$ rapidity interval. Similar fits are performed in other rapidity intervals, allowing the extraction of the coherent exclusive $J/\psi \to \mu^+\mu^-$ yield for each interval.

6 Efficiency and acceptance corrections

The following formula is used to calculate the differential cross section

$$\frac{\mathrm{d}\sigma}{\mathrm{d}y} = \frac{N^{\mathrm{coh}}_{J/\psi\to\mu^+\mu^-}}{A \times \epsilon_C \times BR \times \mathcal{L}_{\mathrm{int}} \times \Delta y} \, , \tag{1}$$

where Δy is the width of the rapidity interval, $\mathcal{L}_{\mathrm{int}}$ is the integrated luminosity of the data sample and BR is the $J/\psi \to \mu^+\mu^-$ branching fraction, the ϵ_C and A factors are corrections accounting for reconstruction

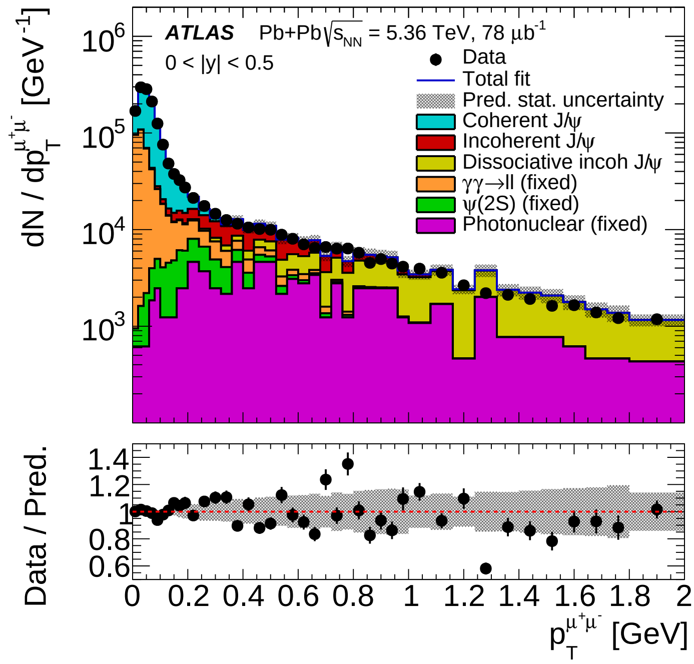

Figure 4 – Exclusive two-track system $p_{\mathrm{T}}^{\mu^+\mu^-}$ distributions in the SR (after relaxing $p_{\mathrm{T}}^{\mu^+\mu^-} < 0.2$ GeV requirement) [14]. Data is show with black markers. Templates from simulation are fitted to data and each contributions to the fit is shown using different color histograms. The total fit result for each rapidity region is shown as a solid blue line. For the calculation of $p_{\mathrm{T}}^{\mu^+\mu^-}$, the muon mass hypothesis is used for each track.

efficiency and acceptance, $N^{\mathrm{coh}}_{J/\psi\to\mu^+\mu^-}$ is the raw yield of coherent $J/\psi \to \mu^+\mu^-$ events extracted from the $p_{\mathrm{T}}^{\mu^+\mu^-}$ fits. The ϵ_C and A correction factors are calculated separately for each rapidity interval.

The acceptance correction factor A allows to correct the cross section measured in the fiducial phase space to the full phase space. It is calculated as the ratio of the number of coherent $J/\psi \to \mu^+\mu^-$ events that fall into the fiducial region to the number of all coherent $J/\psi \to \mu^+\mu^-$ events generated in a given rapidity interval. The rapidity of the J/ψ is calculated using the system of truth muons taken before final state radiation. The fiducial region is defined as two opposite-sign muons after FSR with $p_{\mathrm{T}} > 1$ GeV and $\eta < 2.5$ each, and the two-muon system invariant mass $2.9 < m_{\mu^+\mu^-} < 3.2$ GeV and a transverse momentum $p_{\mathrm{T}}^{\mu^+\mu^-} < 0.2$ GeV.

The reconstruction efficiency correction factor ϵ_C accounts for detector inefficiencies. Its main component is the trigger efficiency scale factor, but is accounts also for track reconstruction efficiency. Detailed study of the trigger efficiency is presented in the following Section 7. The correction factor ϵ_C is defined as the ratio of the number of reconstructed coherent $J/\psi \to \mu^+\mu^-$ events in the fiducial region, to the number of generated events in the same region. The rapidity interval for each event is calculated using the rapidity of the two-muon system. For the numerator the reconstructed two-track system is used, and for the denominator the truth two-muon system after FSR.

7 Trigger efficiency measurement

The L1 TRT trigger efficiency is studied using reference triggers based on the ZDC signal. As the ZDC is independent of the ID it can serve as an unbiased reference for the TRT FastOR trigger. The reference trigger at L1 requires at least one neutron to be detected in one of the ZDC arms and no activity in the other ZDC arm. The total transverse energy on the calorimeters is required to be below 200 GeV. At HLT the event is required to have no more than 5 GeV transverse energy in the FCal and at least one ID track with $p_{\mathrm{T}} > 0.2$ GeV. The efficiency of this HLT trigger is found to be above 99%.

The L1 TRT trigger efficiency does not depend strongly on the track p_{T} above 1 GeV. The efficiency of this trigger is observed to depend mainly on track η. In the study six $|\eta|$ regions are defined. $|\eta| < 0.7$ corresponds to the TRT barrel region. The transition region between barrel and endcap TRT regions is divided in two $|\eta|$ intervals: $0.7 \le |\eta| < 0.9$ and $0.9 \le |\eta| < 1.1$. The $1.1 \le |\eta| < 1.8$ interval covers the endcap TRT, while $1.8 \leq |\eta| < 2$ and $2 \leq |\eta| < 2.5$ cover the edges of endcap TRT.

As the TRT FastOR performs a simple logical "OR" of electronic signals, it is not possible to determine which one of the two tracks is responsible for the trigger decision. For this reason, the efficiency is studied as a function of $|\eta|$ of both tracks simultaneously.

The offline event selections for the L1 TRT trigger efficiency calculation is similar to that used in the actual $J/\psi \rightarrow \mu^+\mu^-$ analysis. After the selection, for each ($|\eta_1|$, $|\eta_2|$) bin, two separate invariant mass distributions are created. One distribution is created with only the requirement on the reference trigger, and another after requiring both the reference and the L1 TRT triggers to fire. In each bin the $J/\psi \rightarrow \mu^+\mu^-$ and $J/\psi \rightarrow e^+e^-$ yields are also distinguished using fits to the invariant mass distribution, as in the actual $J/\psi \rightarrow \mu^+\mu^-$ analysis (see Section 5.3). The yields of $J/\psi \rightarrow \mu^+\mu^-$ extracted from these fits are used to calculate the efficiency in data. The resulting efficiency is shown in Figure 5 in the left plot. The efficiency is observed to be about 60–90% if at least one muon is found in the TRT

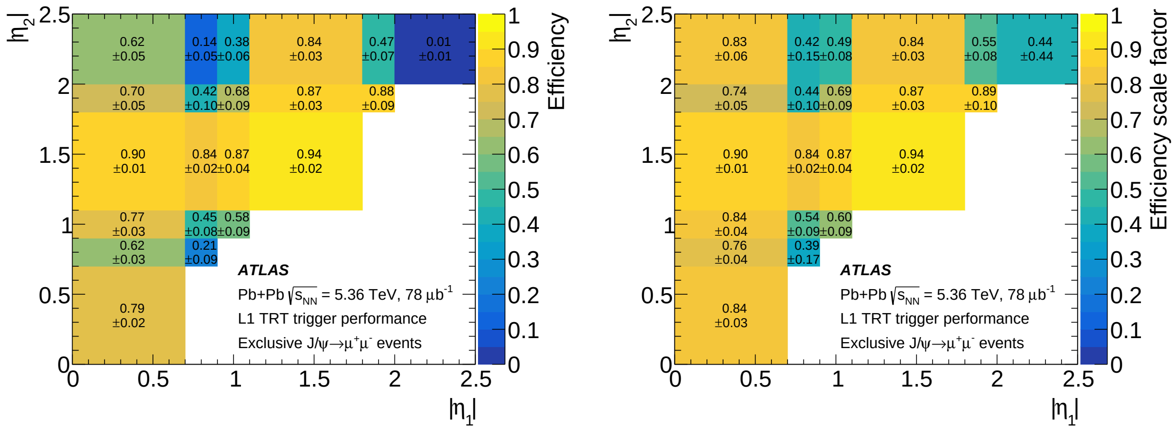

Figure 5 – Left plot shows the L1 TRT trigger efficiency for dimuon events in data as a function of $|\eta_1|$ and $|\eta_2|$ [14]. Right plot shows L1 TRT trigger efficiency scale factors for dimuon events as a function of $|\eta_1|$ and $|\eta_2|$ [14]. Numerical values of trigger efficiency and scale factors are also shown, along with the respective statistical uncertainties.

barrel region, and about 80–90% if at least one muon is in the TRT endcap region. The efficiency drops significantly if one of the muons falls into the transition region or is detected at the edge of the TRT.

The efficiency in simulation is calculated from the $J/\psi \rightarrow \mu^+\mu^-$ MC sample. This allows the calculation of scale factors (SF) depending on $|\eta_1|$ and $|\eta_2|$. The resulting scale factor map is shown in Figure 5 in the right plot. The measured scale factors are used to correct the simulated signal and background MC events. They are applied as weights to the MC events.

8 Systematic uncertainties

Several sources of systematic uncertainty are considered. The most significant sources of systematic uncertainty are: luminosity, L1 TRT trigger efficiency, ID material modeling, methodology used in fits, the shape of the $p_T^{\mu^+\mu^-}$ spectrum for signal, and track veto. The size of each contribution for each rapidity bin is shown in Figure 6. It also shows the statistical uncertainty and the resulting total uncertainty. It is observed that the luminosity uncertainty is the dominant contribution for $|y| < 2$.

The statistical uncertainty on the L1 TRT trigger SF is calculated using the pseudo-experiment method where the SF values are randomly shifted according to the mean and standard deviation of the correction factor.

Systematic uncertainties on the L1 TRT trigger SF account for various changes in the selection criteria described in Section 7. The SF systematic uncertainty is propagated in the nominal analysis by coherently shifting the SF values by one standard deviation and measuring the resulting change in the cross sections. This difference is then taken as a systematic uncertainty.

Uncertainty on ID material modeling reflects assumptions about the geometry of the Inner Detector. It is estimated using different MC samples generated with alternative assumptions of the Inner Detector geometry. In each MC sample, the particles interact slightly differently with the detector and result in

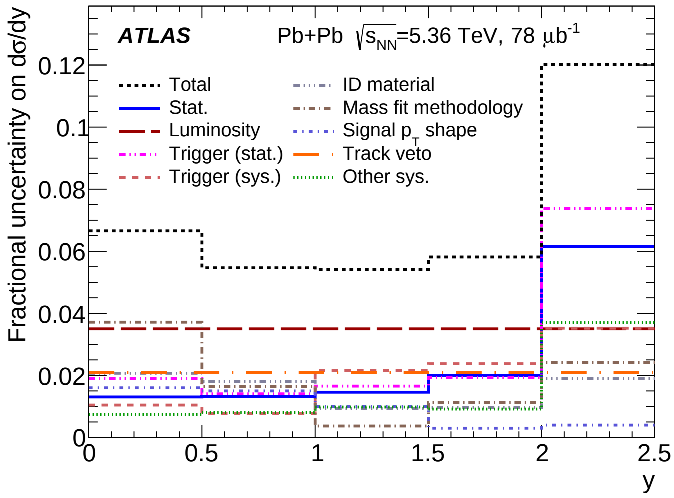

Figure 6 – The total uncertainty of differential cross section measurement for coherent exclusive J/ψ meson production in Pb+Pb UPC at 5.36 TeV as a function of J/ψ rapidity [14]. Breakdown of the individual uncertainty contributions are also shown.

slightly different shapes of the $m_{\mu^+\mu^-}$ and $p_T^{\mu^+\mu^-}$ templates. The difference between the signal yields measured using nominal and varied templates is taken as a systematic uncertainty.

Mass fit methodology uncertainty takes into account an alternative approach to the $p_T^{\mu^+\mu^-}$ fit procedure. In an alternative analysis the $e^+e^-/\mu^+\mu^-$ ratio is not fixed according to the invariant mass fit results, but is fixed according to STARlight predictions instead. The difference between the signal yields measured in the nominal and alternative analysis is taken as a systematic uncertainty.

Sensitivity of the analysis to the coincidence of the $J/\psi \to \mu^+\mu^-$ process with other UPC processes, such as $\gamma\gamma \to e^+e^-$ or coherent $\rho^0 \to \pi^+\pi^-$, is estimated by relaxing the track veto requirement. The track selection is relaxed from exactly two tracks to allow up to four tracks. The difference between the signal yields measured in the analyses with modified and nominal track-veto requirements is taken as a systematic uncertainty.

9 Results

Differential cross sections for the coherent $J/\psi \to \mu^+\mu^-$ process in UPC are calculated from measured yields using Equation 1. Obtained results are presented in Figure 7. The left plot shows measured cross sections compared with several model predictions: STARlight 2.0 and Color Glass Condensate (CGC) models with and without shape fluctuations. All models use HERA $\gamma p \to J/\psi p$ data as an input. The CGC-based model including the additional shape fluctuations is found to provide the best description of the data (with a p-value of 0.8, calculated from the chi-square statistic). In the right plot of Figure 7 the results of this measurement are extrapolated down to $\sqrt{s_{\rm NN}} = 5.02$ TeV and compared with ALICE [8,9], CMS [11] and LHCb [13] measurements. The result of this measurement agrees well with other measurements at higher rapidities. A significant tension between this measurement and ALICE results is observed at mid-rapidity ($0 < y < 0.8$).

10 Conclusions

The first measurement of coherent J/ψ production in ultraperipheral heavy-ion collisions in ATLAS at the LHC is presented. It uses 78 μb^{-1} of Pb+Pb data recorded in 2023 at $\sqrt{s_{\rm NN}} = 5.36$ TeV. Events were selected with a special trigger requiring signal from the ATLAS Transition Radiation Tracker (TRT) at Level 1. The analysis focuses on $J/\psi \to \mu^+\mu^-$ decay channel, while $J/\psi \to e^+e^-$ is treated as background due to significant distortions of electrons in the detector material. This analysis measures the differential cross section for coherent exclusive J/ψ production in UPC within the $|y| < 2.5$ rapidity interval. The results are compared with theoretical predictions and with previous LHC Run 2 measurements after extrapolation to $\sqrt{s_{\rm NN}} = 5.02$ TeV. A model based on the Color Glass Condensate with nucleon shape fluctuations is found to be compatible with the measured cross sections. Significant tension is observed

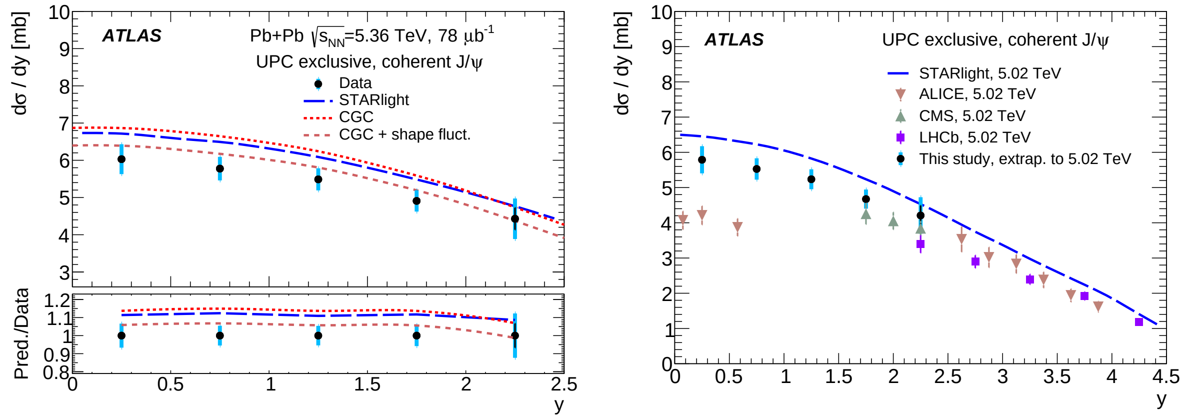

Figure 7 – The left plot shows differential cross section for coherent exclusive J/ψ meson production in Pb+Pb UPC at $\sqrt{s_{\rm NN}} = 5.36$ TeV as a function of J/ψ rapidity (averaged over both sides) [14]. Data (points) are compared with several model predictions: STARlight 2.0, and two versions of a Color Glass Condensate (CGC) model [15,16] (different dashed lines). For each measurement, the thin black vertical bar represents the statistical uncertainty, and the thick blue bar represents the total uncertainty (with statistical and systematic uncertainties added in quadrature). The right plot shows differential cross section for coherent J/ψ meson production in Pb+Pb UPC at 5.02 TeV as a function of J/ψ rapidity [14]. Displayed are previous results from the ALICE [8,9], CMS [11] and LHCb [13] experiments, together with the result of this analysis extrapolated to 5.02 TeV. Data (points) are compared with STARlight predictions (dashed line).

with ALICE data at mid-rapidity ($0 < y < 0.8$) when extrapolating this measurement to $\sqrt{s_{\rm NN}} =$ 5.02 TeV.

Acknowledgments

This work was realized as part of the NCN PRELUDIUM BIS 4 project 2022/47/O/ST2/00148. Research project partly supported by the programme “Excellence initiative – research university” project no 9722 for the AGH University of Krakow.

NATIONAL SCIENCE CENTRE POLAND

AGH

RESEARCH UNIVERSITY EXCELLENCE INITIATIVE

References

1. A. J. Baltz. The Physics of Ultraperipheral Collisions at the LHC. *Phys. Rept.*, 458:1–171, 2008.
2. S. Klein and P. Steinberg. Photonuclear and two-photon interactions at high-energy nuclear colliders. *Annu. Rev. Nucl. Part. Sci.*, 70(1):323–354, 2020.
3. STAR Collaboration. Exclusive J/ψ, ψ(2s), and e+e− pair production in Au+Au ultraperipheral collisions at the BNL Relativistic Heavy Ion Collider. *Phys. Rev. C*, 110(1):014911, 2024.
4. ALICE Collaboration. Coherent J/ψ photoproduction in ultra-peripheral Pb-Pb collisions at $\sqrt{s_{NN}} = 2.76$ TeV. *Phys. Lett. B*, 718:1273–1283, 2013.
5. ALICE Collaboration. Charmonium and e^+e^- pair photoproduction at mid-rapidity in ultra-peripheral Pb-Pb collisions at $\sqrt{s_{NN}}$=2.76 TeV. *Eur. Phys. J. C*, 73(11):2617, 2013.
6. ALICE Collaboration. Coherent ψ(2S) photo-production in ultra-peripheral Pb Pb collisions at $\sqrt{s}_{NN} = 2.76$ TeV. *Phys. Lett. B*, 751:358–370, 2015.
7. CMS Collaboration. Coherent J/ψ photoproduction in ultra-peripheral PbPb collisions at $\sqrt{s_{NN}} =$ 2.76 TeV with the CMS experiment. *Phys. Lett. B*, 772:489–511, 2017.
8. ALICE Collaboration. Coherent J/ψ photoproduction at forward rapidity in ultra-peripheral Pb-Pb collisions at $\sqrt{s_{NN}} = 5.02$ TeV. *Phys. Lett. B*, 798:134926, 2019.

9. ALICE Collaboration. Coherent J/ψ and ψ' photoproduction at midrapidity in ultra-peripheral Pb-Pb collisions at $\sqrt{s_{\rm NN}} = 5.02$ TeV. *Eur. Phys. J. C*, 81(8):712, 2021.
10. ALICE Collaboration. Energy dependence of coherent photonuclear production of J/ψ mesons in ultra-peripheral Pb-Pb collisions at $\sqrt{s_{\rm NN}} = 5.02$ TeV. *JHEP*, 10:119, 2023.
11. CMS Collaboration. Probing Small Bjorken-x Nuclear Gluonic Structure via Coherent J/ψ Photoproduction in Ultraperipheral Pb-Pb Collisions at sNN=5.02 TeV. *Phys. Rev. Lett.*, 131(26):262301, 2023.
12. LHCb Collaboration. Study of coherent J/ψ production in lead-lead collisions at $\sqrt{s_{\rm NN}} = 5$ TeV. *JHEP*, 07:117, 2022.
13. LHCb Collaboration. Study of exclusive photoproduction of charmonium in ultra-peripheral lead-lead collisions. *JHEP*, 06:146, 2023.
14. ATLAS Collaboration. Measurement of coherent exclusive $J/\psi \to \mu^+\mu^-$ production in ultraperipheral Pb+Pb collisions at $\sqrt{s_{\rm NN}} = 5.36$ TeV with the ATLAS detector. 9 2025.
15. H. Mäntysaari, F Salazar, and B. Schenke. Nuclear geometry at high energy from exclusive vector meson production. *Phys. Rev. D*, 106(7):074019, 2022.
16. H. Mäntysaari, F Salazar, and B. Schenke. Energy dependent nuclear suppression from gluon saturation in exclusive vector meson production. *Phys. Rev. D*, 109(7):L071504, 2024.
17. ATLAS Collaboration. The ATLAS Experiment at the CERN Large Hadron Collider. *JINST*, 3:S08003, 2008.
18. ATLAS Collaboration. The ATLAS experiment at the CERN Large Hadron Collider: a description of the detector configuration for Run 3. *JINST*, 19:P05063, 2024.
19. ATLAS Collaboration. The TRT Fast-OR Trigger. ATL-INDET-PUB-2009-002, 2009.
20. ATLAS Collaboration. Performance of the ATLAS Transition Radiation Tracker in Run 1 of the LHC: tracker properties. *JINST*, 12:P05002, 2017.
21. S. R. Klein, J. Nystrand, J. Seger, Y. Gorbunov, and J. Butterworth. STARlight: A Monte Carlo simulation program for ultra-peripheral collisions of relativistic ions. *Comput. Phys. Commun.*, 212:258–268, 2017.
22. C. Bierlich et al. A comprehensive guide to the physics and usage of PYTHIA 8.3. *SciPost Phys. Codeb.*, 2022:8, 2022.
23. ATLAS Collaboration. Exclusive dimuon production in ultraperipheral Pb+Pb collisions at $\sqrt{s_{\rm NN}} = 5.02$ TeV with ATLAS. *Phys. Rev. C*, 104:024906, 2021.
24. D. J. Lange. The EvtGen particle decay simulation package. *Nucl. Instrum. Meth. A*, 462:152–155, 2001.
25. N. Davidson, T. Przedzinski, and Z. Was. PHOTOS interface in C++: Technical and Physics Documentation. *Comput. Phys. Commun.*, 199:86–101, 2016.
26. H1 Collaboration. Elastic and Proton-Dissociative Photoproduction of J/psi Mesons at HERA. *Eur. Phys. J. C*, 73(6):2466, 2013.